CRYSTAL GROWTH & DESIGN

pubs.acs.org/crystal

Article

Morphology and Growth Habit of the New Flux-Grown Layered Semiconductor $KBiS_2$ Revealed by Diffraction Contrast Tomography

Kejian Qu, Hrishikesh Bale, Zachary W. Riedel, Junehu Park, Leilei Yin, André Schleife, and Daniel P. Shoemaker*

Cite This: *Cryst. Growth Des.* 2022, 22, 3228−3234

Read Online

ACCESS | Metrics & More | Article Recommendations | Supporting Information

ABSTRACT: Single crystals of rhombohedral $KBiS_2$ were synthesized for the first time, and the structure, growth habit, and properties of this layered semiconductor are presented. The single crystals form from a reactive K_2S_5 salt flux and are still embedded in the residual flux, without removal from the reaction vessel throughout the whole study. Laboratory diffraction contrast tomography (LabDCT) was used to identify the crystalline phase, orientation, and microstructure of the crystals. Meanwhile, powder and single-crystal X-ray diffraction were used to determine detailed crystallographic information. The morphology of the crystalline assemblies observed by absorption contrast tomography reveals screw-dislocation-driven growth to be the dominant mechanism. First-principles electronic structure simulations predict rhombohedral $KBiS_2$ to be a semiconductor with an indirect band gap, which was confirmed by experiment. This study demonstrates how nondestructive tomographic imaging and 3D crystallography methods can lead to advances in discovering new materials and studying crystal growth mechanisms.

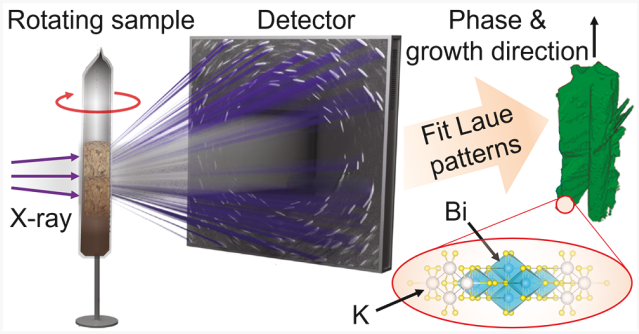

INTRODUCTION

The discovery of new inorganic materials is sustained by the growth of high-quality single crystals that enable robust characterization of their functional properties and permit structure solution from single-crystal diffraction. The most effective crystal growth occurs from liquids or gases, based on enigmatic growth mechanisms that are especially tantalizing in the grand challenge of obtaining metastable materials by extracting them from an aggressive growth medium. Reactions in molten fluxes can lead to such kinetically trapped metastable phases unobtainable by a direct combination of elements,[1] and these methods have proven to be prolific in producing new chalcogenide materials in particular.[2] These compounds are typically narrow-gap semiconductors, and heavy elements lead to strong spin−orbit coupling, which can lead to topologically protected gaps, such as in $TlBiS_2$[3] and Bi_2Se_3.[4] Given the nascent field of crystal growth for nontrivial topology, the identification and high-quality growth of these materials are invaluable.

Unfortunately, the reaction vessels obscure the progression of phase nucleation, growth, and transformation. Some characterizations of flux systems *in situ* have provided views of the crystallization and dissolution of phases in reactive fluxes, in particular by powder diffraction,[5,6] but these methods are poorly suited to probe growths with large crystals.

Here, using the case of a novel flux-grown layered semiconductor crystal, we show how a combination[7] of high-resolution X-ray absorption contrast tomography[8,9] and diffraction contrast tomography[10,11] can be applied to identify previously undiscovered materials with a simultaneous view of the crystal morphology and growth habit. Since the Laue pattern indexation can be quickly checked against known crystal structures, a set of "unmatched" crystals was quickly identified, and the material was determined to be the new layered semiconductor $KBiS_2$, still embedded in the flux. Conducting the entire analysis non-destructively enables an investigation of the crystals in their native environment while the samples are preserved for further subsequent correlative characterization.

Understanding the growth of crystalline materials requires observing the growth habit and grain orientations. Traditional absorption X-ray tomography provides orientation indirectly by facets seen in the density contrast.[12−14] Identifying crystalline phases and their orientations requires diffraction information, which is possible by additionally interrogating the Laue diffraction pattern during sample rotation, as embodied in X-ray diffraction contrast tomography (DCT).[15,16] Diffraction

Received: January 19, 2022
Revised: March 16, 2022
Published: March 31, 2022

https://doi.org/10.1021/acs.cgd.2c00078
Cryst. Growth Des. 2022, 22, 3228−3234

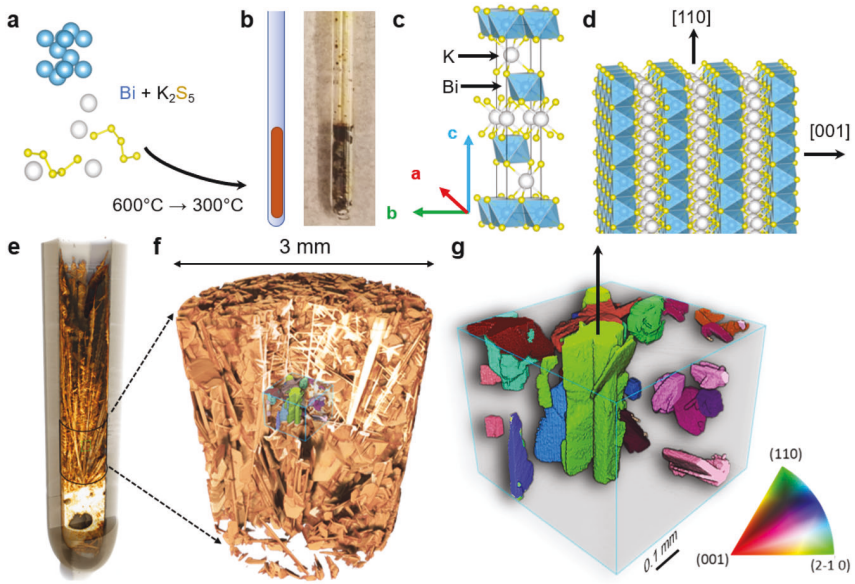

Figure 1. (a) Flux reaction schematics. Details of the synthesis can be found in the Experimental Section. (b) Schematic and image of the sample in a quartz tube after the reaction. The outer tube diameter is 5 mm. (c) Unit cell of rhombohedral $KBiS_2$. (d) [110] and [001] directions in layered rhombohedral $KBiS_2$ crystals. (e) Absorption contrast tomography of the sample, where the outside gray region is the glass tube with a wall thickness of 1 mm. A movie of the whole sample, including the glass tube, can be found in the Supporting Information. (f) Absorption contrast tomography corresponding to the region indicated in (e), with a portion cut to show the needle-shaped crystals. Another high-resolution scan movie in the Supporting Information shows this region in detail. The central volume in color was used for diffraction tomography study. (g) LabDCT picture in inverse pole figure format with the largest central needle-shaped grain in the [110] direction, indicated with the upward arrow.

contrast tomography can be accomplished even with a laboratory X-ray source (LabDCT) instead of one of the few synchrotron sources.[17−19] While the DCT method has been used to map grain orientations (with resolutions of around 50 μm) in Ti,[20,21] AlCu,[17] and Zn−Mg alloys,[22] with synchrotron and conventional X-ray tube sources, those studies were on freestanding materials with simple structures. The utility of DCT for emerging materials, especially novel crystalline materials intact within their synthesis environment, has never been shown.

In this study, we take advantage of the grain visualization capabilities of DCT in combination with the wealth of single-crystal Laue diffraction data to confirm the crystal size, shape, orientation and identity simultaneously on a much more complex sample. From absorption contrast tomography on the same sample, we identify needle and plate morphologies of rhombohedral $KBiS_2$ that can be attributed to different stages of nucleation and growth, suggesting a screw-dislocation-driven growth mechanism.[23] Applying these measurement techniques to future *in situ* studies in extreme environments (especially in aggressive chemical potentials) will allow short-lived, kinetically trapped phases to be obtained, which should accelerate the discovery of new metastable materials.

EXPERIMENTAL SECTION

Synthesis. The flux for $KBiS_2$ crystal growth is K_2S_5, which was synthesized by a stoichiometric reaction of potassium (0.356 g, 99%) and sulfur (0.729 g, 99.9%). The potassium chunk was loaded into a one-side-open small quartz tube, which was loaded into a larger quartz tube with sulfur at the bottom to avoid direct contact between sulfur and potassium. The larger quartz tube was sealed under vacuum. After the temperature was ramped up to 400 °C for 18 h, the sample was kept at 400 °C for another 18 h to allow sulfur to be fully transported and react with potassium to form K_2S_5. Next, flux reactions were conducted in fused silica tubes with Bi shots (0.104 g, 99.9%, around 10 × 2 × 2 mm^3) in K_2S_5 (0.236 g). The flux reaction mixtures contained a nominal stoichiometry of $2K_2S_5$ + Bi, and the temperatures were ramped to 600 °C in 6 h, held for 6 h, and then cooled to 300 °C for 50 h, and then the samples were quenched in water to ensure that the remaining flux was amorphous.

Tomography. The sealed tubes were first examined by X-ray absorption contrast tomography using a Rigaku CTLab GX130 machine at the Beckman Institute at the University of Illinois to verify the presence of crystals in the flux. High-resolution absorption contrast tomography (ACT) and LabDCT measurements were carried out using a ZEISS Xradia 620 Versa X-ray microscope (Carl Zeiss X-ray Microscopy, Dublin, CA). The objective-based dual-magnification setup of the X-ray microscope allowed zooming into the interior region of interest at a higher resolution of 1 μm/voxel without the need for cutting samples to smaller sizes as would be needed on a conventional microCT setup. A full field of view scan collected at 6 μm/voxel provides a full overview of the tube, enabling us to pinpoint local regions of interest for high-resolution absorption and diffraction contrast tomography. For ACT, 1601 projections were obtained with a 3 s exposure at an X-ray energy of 160 kV at 10 W, using a HE2 high-energy filter. The total run time was about 2 h. The data were reconstructed using the microscope's proprietary 3D reconstruction software (ZEISS XMReconstructor), which is based on the FDK reconstruction algorithm. Diffraction contrast tomography was performed at 160 kV in the Laue focusing geometry, where the source and detector were aligned equidistant from the sample. A set of 181 diffraction projections were collected over a 360° rotation of the sample, each with an exposure of 180 s, making the total run time about 9 h. The interior region of interest for diffraction contrast tomography was determined from 3D reconstructed absorption contrast tomography data using a scout-and-zoom method. 3D crystallographic reconstruction was carried out with a dedicated 3D grain mapping software[17] supplied with the microscope (GrainMapper3Dv3.0; Xnovo Technology ApS, Denmark). For indexation of the crystal structures, a refined crystal parameter file was imported on the basis of XRD measurements of isolated crystals of rhombohedral $KBiS_2$. An overlay of the grain reconstruction and the absorption data and 3D visualization

https://doi.org/10.1021/acs.cgd.2c00078
Cryst. Growth Des. 2022, 22, 3228−3234

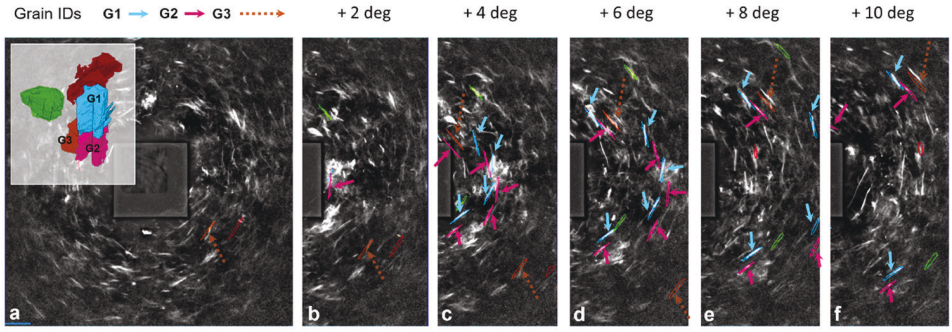

Figure 2. (a) Laue diffraction patterns collected from the region of interest indicated in Figure 1f,g. For the sake of clarity, only three prominent grains and their corresponding Laue reflections are highlighted. (b–f) Selected Laue diffraction patterns where the sample was rotated in 2° steps about the central axis of the glass tube. The outlined reflections correspond to the three grains with the colors assigned as unique identifiers. The tracking of reflections at the expected locations during sample rotation confirms the orientation determination. G1 and G2 have reflections that appear in the same frames because they are fragments of a much longer, crystallographically aligned needle. A movie of raw Laue diffraction spots as the sample was rotated about its vertical axis (without background subtraction) is given in the Supporting Information.

and analysis were performed with Dragonfly Pro software (Object Research Systems, Montreal, Canada).

Crystal Structure Determination. Duplicate samples were made to obtain individual single crystals, using the same stoichiometry and heating sequence as detailed above. Crystals were collected by dissolving the flux in distilled water. Single-crystal X-ray diffraction on a Bruker D8 Venture Duo instrument gave a structure of $KBiS_2$, with the $TlBiS_2$ structure type in space group $R\bar{3}m$. Powder X-ray diffraction was performed to verify that the crystalline product was a single phase. Stoichiometric starting materials ($4Bi + K_2S_5 + K_2S_3$), where K_2S_3 was synthesized in the same way as for K_2S_5 with stoichiometric K and S, produced cubic $KBiS_2$. The full refinement results and structures are given in Table S1 and Figure S1 in the Supporting Information.[24]

UV–vis–NIR Measurement. UV–vis–NIR measurements were carried out for ground powders using a Varian Cary 5G instrument at the Materials Research Laboratory at University of Illinois, and the reflectance vs wavelength data were converted and linearly fitted with the Tauc method.[25] R_∞ is the diffuse reflectance of the sample, and $F(R_\infty)$ is the Kubelka–Munk function, defined as $F(R_\infty) = (1 - R_\infty)^2/2R_\infty$. In the Tauc method, $(F(R_\infty)\cdot h\nu)^{1/2} = B(h\nu - E_g)$, where $h\nu = 1239.7/\lambda$ in units of eV, wavelength λ in units of nm and B being a constant. Finally, linear regression was performed for the linear portion of the $(F(R_\infty)\cdot h\nu)^{1/2}$ versus energy $h\nu$ curve, and E_g is the intercept of the straight line with the horizontal axis, which is around 1.21 eV.

Band Structure Calculation. We used the Vienna Ab-Initio Simulation Package (VASP)[26–28] to compute the electronic structure and optical spectra within first-principles density functional theory (DFT). The generalized-gradient approximation by Perdew, Burke, and Ernzerhof (PBE)[29] was used to describe exchange and correlation and compared to the hybrid HSE06 functional by Heyd, Scuseria, and Ernzerhof.[30] The projector-augmented wave (PAW) method[31] was used to describe the electron–ion interaction, and Kohn–Sham wave functions were expanded into a plane-wave basis up to a kinetic-energy cutoff of 500 eV. The spin–orbit interaction was taken into account in a fully noncollinear approach.[32] These simulations were performed for the atomic coordinates of the conventional cell provided by Materials Project (mp-ID 1223443)[33,34] that we converted to a primitive unit cell using AFLOW/ACONVASP.[35] We subsequently relaxed the atomic coordinates until all forces were less than 5 meV/Å. We used a $12 \times 12 \times 12$ Γ-centered k-point grid for the Brillouin zone integration in computing the PBE electronic structure, a Γ-centered $4 \times 4 \times 4$ grid for the HSE06 data, and a Γ-centered $16 \times 16 \times 16$ grid for optical spectra.

RESULTS AND DISCUSSION

The flux reaction schematics and the crystal structure of rhombohedral $KBiS_2$, along with the tomography setup and both absorption contrast and diffraction contrast tomography data, are all shown in Figure 1. Figure 1a shows the reaction schematic, where Bi and K_2S_5 flux are loaded into a fused silica tube, shown in Figure 1b. They were reacted at 600 °C and slowly cooled to 300 °C. The tube has a 3 mm inner diameter and 1 mm wall thickness, as can be seen in Figure 1e, typical for single-crystal growth in reactive fluxes with moderate vapor pressures. The region used for tomography study is at the bottom portion of the tube, embedded in flux, and is optically opaque. The unit cell of the crystalline product $KBiS_2$ is shown in Figure 1c. The density contrast reconstruction of the entire tube in the tomographic region is shown in Figure 1f with a density cutoff chosen so that only the Bi-containing crystals are visible, while the flux is transparent. Needle- and plate-shaped crystals with some dimensions greater than 1 mm are evident, and powder diffraction of replica samples, with all crystals ground together, confirmed that they are the same phase (Figure S1).[24] Initially, no fit to the Laue patterns could be obtained by DCT using the reported crystal structures of phases in the K–Bi–S system: $KBiS_2$,[36–39] KBi_3S_5,[40] $K_2Bi_8S_{13}$,[41] $KBi_{6.33}S_{10}$,[41] and $K_9Bi_{13}S_{24}$.[42] However, single-crystal diffraction data of crystals from a replica sample provided a structure solution of a new rhombohedral phase of $KBiS_2$, previously unreported in the Inorganic Crystal Structure Database (ICSD), which indexed the DCT Laue data with a high completeness value.[17] After our analysis was complete, this phase was also reported in powder form.[43]

Figure 1g shows the subset of crystals with which Laue patterns were obtained, colored with respect to their orientations on the basis of the inverse pole figure (IPF) reference shown on the bottom right. The largest needle passing through the center of the volume has the (110) plane normal to the vertical direction and the most complete matching to the Laue pattern. We focus the bulk of our analysis on this grain. The orientation of the central needle-shaped grain is with the [110] direction upward, shown for the $KBiS_2$ structure in Figure 1g.

Figure 2a shows raw diffraction patterns obtained in the DCT scan, where reflections from a large number of crystals are observed. Such a large number of reflections is a result of the polychromatic X-ray diffraction from the entire illuminated cross-section of the sample, not just from the inner region of interest (the cube volume in Figure 1g). A diffuse background from the amorphous flux and glass wall was subtracted but can be seen in the supplementary movie in the Supporting Information.[24] Despite the presence of extraneous grains outside the region of interest, and the expected absorption of weak

https://doi.org/10.1021/acs.cgd.2c00078
Cryst. Growth Des. 2022, 22, 3228–3234

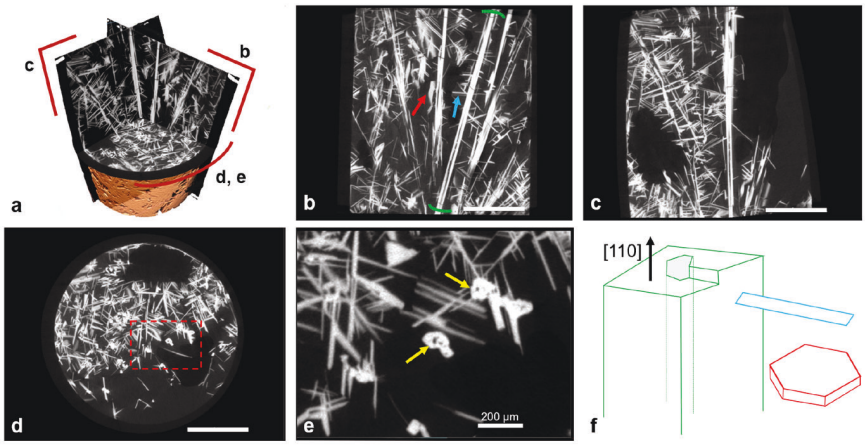

Figure 3. (a) 3D multiplanar view of the absorption contrast tomography data. (b–d) 2D planar views indicated in (a), where the bars all correspond to 1 mm. (e) Enlarged view of the red square region in (d) highlighting hollow channels in crystals with arrows. (f) Schematics of needle, plate, and dendrite, which are indicated in (b) with green arcs, red arrow, and blue arrow, respectively.

diffraction peaks by other grains or the tube wall, many strong reflections from the region of interest are successively tracked as the sample is rotated. Correct peak indexing is verified by tracking the diffraction spots from frame to frame, as the sample is rotated, shown in Figure 2b–f. Two grains, G1 and G2, have reflections that precess as expected (marked with short arrows) as the sample is rotated by 10° over five frames. These reflections are primarily of {110} and {114} character, as indexed in Figure S3 in the Supporting Information.[24] The ability to index the central grain, despite the presence of additional peaks and absorption from nearby grains, is a testament to the robustness of the grain reconstruction algorithm.[17] The grains G1 and G2 belong to a single needle with nominally the same crystal orientation, as can be seen in Figure 1g. High-resolution absorption contrast tomography images revealed that these long, needle-shaped crystals have occasional cross-sectional breaks along their length. The angular orientation sensitivity of DCT allows the detection of a subtle change in orientation at the breaks as distinct pairs of reflections, which is evidenced by the different locations of G1 and G2 reflections in Figure 2. Corresponding {*hkl*} and IPF indexations are shown in Figure S3, for a total of 26 grains indexed within the region of interest.[24]

We solved our unknown phase as rhombohedral $KBiS_2$, an ordered rock salt derived phase, in space group $R\bar{3}m$ with a = 4.12 Å and c = 22.09 Å. This is in contrast with the established polymorph, cubic rock salt $KBiS_2$,[36] with K^+ and Bi^{3+} being randomly mixed and a = 6.04 Å. The rhombohedral phase has layered K and Bi (001) planes (Figure 1d), which correspond to (111) planes in the rock salt structure. This type of rhombohedral $R\bar{3}m$ ordering can also be seen in other ABQ_2 materials such as $AgSbTe_2$, in which both randomized NaCl type ($Fm\bar{3}m$) and ordered rhombohedral ($R\bar{3}m$) structures, together with other ordered structures, have been confirmed experimentally.[44,45]

In this case, DCT Laue diffraction was able to confirm the structure of the crystals grown but not to solve a new unknown structure. In addition to the background from flux, too many diffraction spots were generated by different orientations of different crystal grains. Thus, more insights into the growth mechanism of the rhombohedral $KBiS_2$ can help the growth of larger but fewer grains, ideally making it possible to solve the crystal structure from DCT data alone generated from very few large crystals.

Tomographic slices are viewed in absorption contrast mode in Figure 3, primarily focused on the long needles in the center of the sample, which, due to their unbroken lengths and protruding dendrites, can be assumed to be among the first large grains to form. Secondary and tertiary dendrites can be seen attached to the primary needle crystals that originate from the bottom of the reaction tube, with this convergence being most apparent in Figure 3b. The cross-sectional views of the needles in Figure 3d,e reveal hollow centers that likely arise from screw-dislocation-driven spiral growth[22,23] when the dislocation strain field energy is balanced by the creation of an internal surface energy.

Typically, screw-dislocation-driven growth will dominate when the supersaturation in the solution is relatively low,[46] which is observed here when the solution was in its initial period of slow cooling. From classical theory of dislocation-driven crystal growth,[47] the radius of the hollow channel r is related to the Burgers vector of dislocation b as $r = \frac{\mu b^2}{8\pi^2\gamma}$, where μ is the shear modulus and γ is the surface energy density. Here the Eshelby twist[48] is not included, since for this case, the outer radius of the needle-shaped crystals is significantly larger than the inner radius. The formula above indicates a comparatively small surface energy for this synthesis, since the crystal is grown from a polysulfide flux with a similar composition.

The preferred [110] growth direction likely results from the easy addition of all three ions to this plane, rather than termination planes of a single ionic type, as would be the case for [001] (shown in Figure 1d). In this way, all ions can precipitate simultaneously. At the same time, the growth direction *inside the vessel* is aligned vertically—this insight is only possible by non-invasive tomography of the material inside the glass tube, while it also reveals the interior pore structure of the grains.

Some plate-shaped crystals can also be seen, which is the result of layer-by-layer growth, when the supersaturation is in a moderate regime.[23,49] Finally, when the supersaturation increases further, especially in the late cooling period, dendrites will form. Overall, the screw-dislocation-driven growth dominated the initial period when the needles formed, and plates could only form starting from a later period, at which time there was not much empty space available. This is the reason plate-shaped crystals larger than 1 mm × 0.5 mm are not observed, while the needle-shaped crystals in our tomography data are

https://doi.org/10.1021/acs.cgd.2c00078
Cryst. Growth Des. 2022, 22, 3228–3234

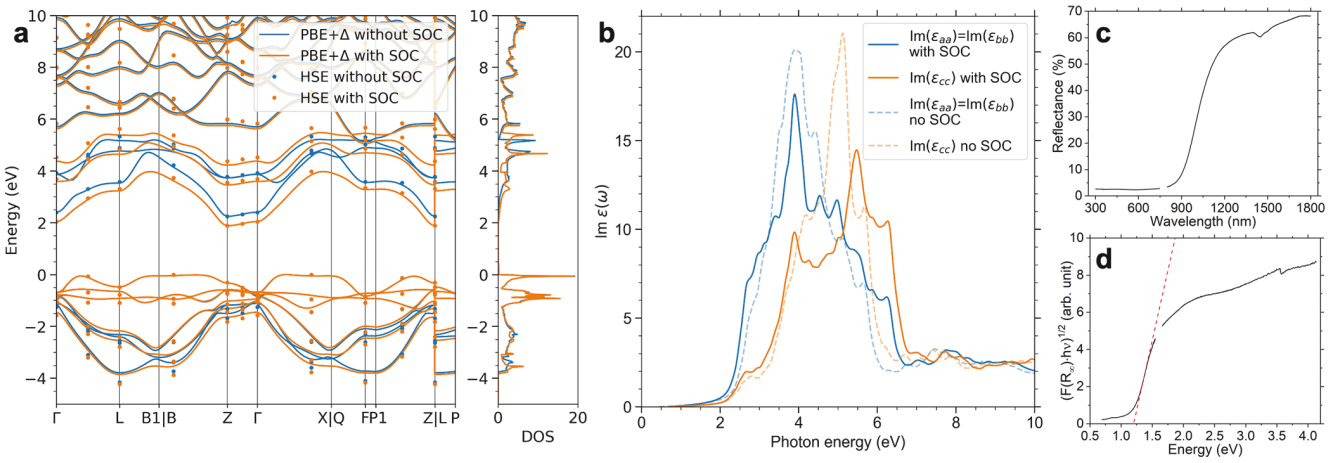

Figure 4. (a) Kohn–Sham electronic band structure (left) and density of states (right, in eV^{-1} normalized to 1 formula unit) from density functional theory simulations, with and without spin–orbit coupling. Results from the hybrid HSE06 exchange-correlation functional (dots) agree to within 0.5 eV with scissor-shifted (Δ = 0.73 eV) PBE data (lines). (b) Calculated imaginary part of the frequency-dependent dielectric tensor. Scissor-shifted PBE data with (Δ = 0.73 eV) and without (Δ = 0.44 eV) spin–orbit coupling is compared, illustrating the influence of spin–orbit interactions on the spectral shape, absorption onset, and anisotropy. (c) Experimental UV–vis–NIR diffuse reflectance measurement of powdered $KBiS_2$. (d) UV–vis–NIR data fit with the Tauc method, where the Kubelka–Munk function $F(R_\infty)$ is defined in the Experimental Section. The indirect band gap is 1.21 eV.

longer than 5 mm. Figure 3f shows the schematics of all three types of crystals.

Another crystal growth mechanism that also produces hollow spaces[50] is not in play here, due to the long and thin morphology of rhombohedral $KBiS_2$ crystals with an unvarying radius of the needle-shaped crystals and the hollow core inside. Thus, we believe the needles grew from screw dislocation.

Finally, the electronic band structure of rhombohedral $KBiS_2$ was investigated by both theoretical calculations and ultraviolet–visible–near-infrared (UV–vis-NIR) spectroscopy measurements, and the results are shown in Figure 4. Our Kohn–Sham electronic structure without spin–orbit coupling (SOC), shown in Figure 4a, agrees well with that reported in an earlier work.[43] In addition, we also quantified the influence of spin–orbit coupling and found that including this effect decreases the band gap by about 0.29 eV (DFT-PBE) and 0.36 eV (HSE06). Several of the lowest conduction bands are split by spin–orbit coupling; see Figures S4 and S5 in the Supporting Information.[24] The valence bands between 2 and 4 eV below the Fermi energy are also affected, but to a lesser extent. These splittings also affect the optical properties of the material, as shown in Figure 4b. Overall, the material shows a pronounced optical anisotropy between the optical conductivities ε_{aa} and ε_{cc}, as expected for a layered compound. The aforementioned SOC-driven splitting leads to a spectral broadening of both ε components on the whole, judged by the total width of the peak from ~2–6 eV. The influence of exchange and correlation is significant in this material, as witnessed by the increase in the band gap from 1.15 to 1.88 eV, on comparison of the results from DFT-PBE versus HSE06. UV–vis–NIR spectroscopy was used to measure the band gap using a powder of rhombohedral $KBiS_2$ from replica samples. A Tauc fit to the reflectance data in Figure 4c gives an indirect band gap of is 1.21 eV, shown in Figure 4d. The slight discrepancy of measured band gap in comparison to the calculated band gap is likely due to surface degradation inherent to alkali sulfides in air.

The large crystals obtained here are notably isostructural with rhombohedral $TlBiS_2$. The latter is known to undergo topological phase transitions, and its electronic structure can be tuned by strain,[51,52] temperature,[53] or Se doping on S sites[53] on the basis of DFT calculations. Experiments have demonstrated the tuning of the band structure by temperature[54] and doping.[3,55] For rhombohedral $KBiS_2$, which has a moderate band gap, albeit indirect, the tuning of the band structure via the aforementioned factors is possible, including doping Tl on K sites and introducing strain.

CONCLUSION

In conclusion, we have shown that DCT can be used to identify phases with previously unknown crystal structures, even within bulky reaction vessels, and it can be used to characterize grain orientations. Combining the phase identification of large crystals with their growth mechanisms should lead to future studies that can engineer the growth conditions, such as changing the temperature profile, the starting stoichiometry, etc. in order to obtain the preferred phase and/or morphology. All tomographic analyses were performed without a synchrotron X-ray source and without opening the fused silica tube, showing the possibility of further study on sensitive samples and *in situ* measurements during the growth process over a prolonged experimental period. UV–vis–NIR spectroscopy measurements confirmed rhombohedral $KBiS_2$ to be a semiconductor with an indirect band gap of 1.21 eV, which was corroborated by first-principles calculations. The parallels between the topological insulator candidate $TlBiS_2$ and isostructural $KBiS_2$ can be investigated in detail with subsequent optimization of the crystal growth.

ASSOCIATED CONTENT

Supporting Information

The following files are available free of charge. The Supporting Information is available free of charge at https://pubs.acs.org/doi/10.1021/acs.cgd.2c00078.

Movies giving an overview of the whole tube, the absorption contrast tomography region (Figure 1f), and Laue diffraction with no background deduction (ZIP)

Crystallographic information on rhombohedral $KBiS_2$ from single-crystal XRD, powder XRD and structure for

https://doi.org/10.1021/acs.cgd.2c00078
Cryst. Growth Des. 2022, 22, 3228–3234

both rhombohedral and cubic $KBiS_2$, SEM and microscope pictures of rhombohedral $KBiS_2$ crystals, Laue diffraction rotation tracking with {*hkl*} planes and crystal orientations, DFT-PBE electronic band structure, and HSE06 electronic band structure (PDF)

Accession Codes

CCDC 2143238 contains the supplementary crystallographic data for this paper. These data can be obtained free of charge via www.ccdc.cam.ac.uk/data_request/cif, or by emailing data_request@ccdc.cam.ac.uk, or by contacting The Cambridge Crystallographic Data Centre, 12 Union Road, Cambridge CB2 1EZ, UK; fax: +44 1223 336033.

AUTHOR INFORMATION

Corresponding Author

Daniel P. Shoemaker − *Department of Materials Science and Engineering and Materials Research Laboratory, University of Illinois at Urbana−Champaign, Urbana, Illinois 61801, United States;* orcid.org/0000-0003-3650-7551; Email: dpshoema@illinois.edu

Authors

Kejian Qu − *Department of Physics and Materials Research Laboratory, University of Illinois at Urbana−Champaign, Urbana, Illinois 61801, United States;* orcid.org/0000-0002-7189-537X

Hrishikesh Bale − *Carl Zeiss X-ray Microscopy Inc., Pleasanton, California 94588, United States*

Zachary W. Riedel − *Department of Materials Science and Engineering and Materials Research Laboratory, University of Illinois at Urbana−Champaign, Urbana, Illinois 61801, United States;* orcid.org/0000-0001-5848-5520

Junehu Park − *Department of Materials Science and Engineering and Materials Research Laboratory, University of Illinois at Urbana−Champaign, Urbana, Illinois 61801, United States*

Leilei Yin − *Beckman Institute, University of Illinois at Urbana−Champaign, Urbana, Illinois 61801, United States*

André Schleife − *Department of Materials Science and Engineering and Materials Research Laboratory and National Center for Supercomputing Applications, University of Illinois at Urbana−Champaign, Urbana, Illinois 61801, United States;* orcid.org/0000-0003-0496-8214

Complete contact information is available at: https://pubs.acs.org/10.1021/acs.cgd.2c00078

Notes

The authors declare the following competing financial interest(s): H.B. is employed by Carl Zeiss X-ray Microscopy, Inc.

ACKNOWLEDGMENTS

This work was supported by the US Department of Energy, Basic Energy Sciences (grant No. DE-SC0013897), for Early Career Research. Characterization was performed at the Materials Research Laboratory and Beckman Institute at the University of Illinois. Computational work was supported by the Illinois Materials Research Science and Engineering Center through the National Science Foundation MRSEC program under NSF Award No. DMR-1720633. This work made use of the Illinois Campus Cluster, a computing resource that is operated by the Illinois Campus Cluster Program (ICCP) in conjunction with the National Center for Supercomputing Applications (NCSA) and which is supported by funds from the University of Illinois at Urbana−Champaign. This research is part of the Blue Waters sustained-petascale computing project, which is supported by the National Science Foundation (awards OCI-0725070 and ACI-1238993) and the state of Illinois. Blue Waters is a joint effort of the University of Illinois at Urbana−Champaign and its National Center for Supercomputing Applications.

REFERENCES

(1) Latturner, S. E. Clusters, Assemble: Growth of Intermetallic Compounds from Metal Flux Reactions. *Acc. Chem. Res.* **2018**, *51*, 40−48.

(2) Kanatzidis, M. G. Molten alkali-metal polychalcogenides as reagents and solvents for the synthesis of new chalcogenide materials. *Chem. Mater.* **1990**, *2*, 353−363.

(3) Sato, T.; Segawa, K.; Kosaka, K.; Souma, S.; Nakayama, K.; Eto, K.; Minami, T.; Ando, Y.; Takahashi, T. Unexpected mass acquisition of Dirac fermions at the quantum phase transition of a topological insulator. *Nat. Phys.* **2011**, *7*, 840−844.

(4) Bansal, N.; Kim, Y. S.; Edrey, E.; Brahlek, M.; Horibe, Y.; Iida, K.; Tanimura, M.; Li, G.-H.; Feng, T.; Lee, H.-D.; Gustafsson, T.; Andrei, E.; Oh, S. Epitaxial growth of topological insulator Bi2Se3 film on Si(111) with atomically sharp interface. *Thin Solid Films* **2011**, *520*, 224−229.

(5) Shoemaker, D. P.; Hu, Y.-J.; Chung, D. Y.; Halder, G. J.; Chupas, P. J.; Soderholm, L.; Mitchell, J. F.; Kanatzidis, M. G. In situ studies of a platform for metastable inorganic crystal growth and materials discovery. *Proc. Natl. Acad. Sci. U.S.A* **2014**, *111*, 10922.

(6) Moorhouse, S. J.; Wu, Y.; Buckley, H. C.; O'Hare, D. Time-resolved in situ powder X-ray diffraction reveals the mechanisms of molten salt synthesis. *Chem. Commun.* **2016**, *52*, 13865−13868.

(7) Lu, N.; Kang, J.; Senabulya, N.; Keinan, R.; Gueninchault, N.; Shahani, A. J. Dynamics of particle-assisted abnormal grain growth revealed through integrated three-dimensional microanalysis. *Acta Mater.* **2020**, *195*, 1−12.

(8) Stock, S. X-ray microtomography of materials. *Int. Mater. Rev.* **1999**, *44*, 141−164.

(9) Stock, S. R. Recent advances in X-ray microtomography applied to materials. *Int. Mater. Rev.* **2008**, *53*, 129−181.

(10) Ludwig, W.; Schmidt, S.; Lauridsen, E. M.; Poulsen, H. F. X-ray diffraction contrast tomography: a novel technique for three-dimensional grain mapping of polycrystals. I. Direct beam case. *J. Appl. Crystallogr.* **2008**, *41*, 302−309.

(11) Johnson, G.; King, A.; Honnicke, M. G.; Marrow, J.; Ludwig, W. X-ray diffraction contrast tomography: a novel technique for three-dimensional grain mapping of polycrystals. II. The combined case. *J. Appl. Crystallogr.* **2008**, *41*, 310−318.

(12) Maire, E.; Withers, P. J. Quantitative X-ray tomography. *Int. Mater. Rev.* **2014**, *59*, 1−43.

(13) Salvo, L.; Cloetens, P.; Maire, E.; Zabler, S.; Blandin, J.; Buffiére, J.; Ludwig, W.; Boller, E.; Bellet, D.; Josserond, C. X-ray micro-tomography an attractive characterisation technique in materials science. *Nucl. Instrum. Methods B* **2003**, *200*, 273−286. Proceedings of the E-MRS 2002 Symposium I on Synchrotron Radiation and Materials Science.

(14) Baruchel, J.; Di Michiel, M.; Lafford, T.; Lhuissier, P.; Meyssonnier, J.; Nguyen-Thi, H.; Philip, A.; Pernot, P.; Salvo, L.; Scheel, M. Synchrotron X-ray imaging for crystal growth studies. *Compt. Rend. Phys.* **2013**, *14*, 208−220.

(15) Shahani, A. J.; Xiao, X.; Lauridsen, E. M.; Voorhees, P. W. Characterization of metals in four dimensions. *Mater. Res. Lett.* **2020**, *8*, 462−476.

(16) Ludwig, W.; Reischig, P.; King, A.; Herbig, M.; Lauridsen, E. M.; Johnson, G.; Marrow, T. J.; Buffiére, J. Y. Three-dimensional grain mapping by x-ray diffraction contrast tomography and the use of Friedel pairs in diffraction data analysis. *Rev. Sci. Instrum.* **2009**, *80*, 033905.

(17) Bachmann, F.; Bale, H.; Gueninchault, N.; Holzner, C.; Lauridsen, E. M. 3D grain reconstruction from laboratory diffraction contrast tomography. *J. Appl. Crystallogr.* **2019**, *52*, 643−651.
(18) Holzner, C.; Lavery, L.; Bale, H.; Merkle, A.; McDonald, S.; Withers, P.; Zhang, Y.; Jensen, D. J.; Kimura, M.; Lyckegaard, A.; et al. Diffraction Contrast Tomography in the Laboratory − Applications and Future Directions. *Microscopy Today* **2016**, *24*, 34−43.
(19) Oddershede, J.; Sun, J.; Gueninchault, N.; Bachmann, F.; Bale, H.; Holzner, C.; Lauridsen, E. Non-destructive Characterization of Polycrystalline Materials in 3D by Laboratory Diffraction Contrast Tomography. *Integr. Mater. Manuf. Innov.* **2019**, *8*, 217−225.
(20) Ludwig, W.; King, A.; Reischig, P.; Herbig, M.; Lauridsen, E.; Schmidt, S.; Proudhon, H.; Forest, S.; Cloetens, P.; du Roscoat, S. R.; Buffiére, J.; Marrow, T.; Poulsen, H. New opportunities for 3D materials science of polycrystalline materials at the micrometre lengthscale by combined use of X-ray diffraction and X-ray imaging. *Mater. Sci. Eng., A* **2009**, *524*, 69−76.
(21) Ludwig, W.; King, A.; Herbig, M.; Reischig, P.; Marrow, J.; Babout, L.; Lauridsen, E. M.; Proudhon, H.; Buffière, J. Y. Characterization of polycrystalline materials using synchrotron X-ray imaging and diffraction techniques. *JOM* **2010**, *62*, 22−28.
(22) Moniri, S.; Bale, H.; Volkenandt, T.; Wang, Y.; Gao, J.; Lu, T.; Sun, K.; Ritchie, R. O.; Shahani, A. J. Multi-Step Crystallization of Self-Organized Spiral Eutectics. *Small* **2020**, *16*, 1906146.
(23) Meng, F.; Morin, S. A.; Forticaux, A.; Jin, S. Screw Dislocation Driven Growth of Nanomaterials. *Acc. Chem. Res.* **2013**, *46*, 1616−1626.
(24) The Supporting Information is available online.
(25) Makuła, P.; Pacia, M.; Macyk, W. How To Correctly Determine the Band Gap Energy of Modified Semiconductor Photocatalysts Based on UV-Vis Spectra. *J. Phys. Chem. Lett.* **2018**, *9*, 6814−6817.
(26) Kresse, G.; Joubert, D. From ultrasoft pseudopotentials to the projector augmented-wave method. *Phys. Rev. B* **1999**, *59*, 1758−1775.
(27) Kresse, G.; Furthmüller, J. Efficient iterative schemes for ab initio total-energy calculations using a plane-wave basis set. *Phys. Rev. B* **1996**, *54*, 11169−11186.
(28) Gajdoš, M.; Hummer, K.; Kresse, G.; Furthmüller, J.; Bechstedt, F. Linear optical properties in the projector-augmented wave methodology. *Phys. Rev. B* **2006**, *73*, 045112.
(29) Perdew, J. P.; Burke, K.; Ernzerhof, M. Generalized Gradient Approximation Made Simple. *Phys. Rev. Lett.* **1996**, *77*, 3865−3868.
(30) Heyd, J.; Scuseria, G. E.; Ernzerhof, M. Erratum: "Hybrid functionals based on a screened Coulomb potential" [J. Chem. Phys. 118, 8207 (2003)]. *J. Chem. Phys.* **2006**, *124*, 219906.
(31) Blöchl, P. E. Projector augmented-wave method. *Phys. Rev. B* **1994**, *50*, 17953−17979.
(32) Steiner, S.; Khmelevskyi, S.; Marsmann, M.; Kresse, G. Calculation of the magnetic anisotropy with projected-augmented-wave methodology and the case study of disordered $Fe_{1-x}Co_x$ alloys. *Phys. Rev. B* **2016**, *93*, 224425.
(33) Jain, A.; Ong, S. P.; Hautier, G.; Chen, W.; Richards, W. D.; Dacek, S.; Cholia, S.; Gunter, D.; Skinner, D.; Ceder, G.; Persson, K. a. The Materials Project: A materials genome approach to accelerating materials innovation. *APL Mater.* **2013**, *1*, 011002.
(34) Ong, S. P.; Richards, W. D.; Jain, A.; Hautier, G.; Kocher, M.; Cholia, S.; Gunter, D.; Chevrier, V. L.; Persson, K. A.; Ceder, G. Python Materials Genomics (pymatgen): A robust, open-source python library for materials analysis. *Comput. Mater. Sci.* **2013**, *68*, 314−319.
(35) Setyawan, W.; Curtarolo, S. High-throughput electronic band structure calculations: Challenges and tools. *Comput. Mater. Sci.* **2010**, *49*, 299−312.
(36) Boon, J. W. The crystal structure of NaBiS2 and KBiS2. *Rec. Trav. Chim. Pays-Bas* **1944**, *63*, 32−34.
(37) Rosales, B. A.; White, M. A.; Vela, J. Solution-Grown Sodium Bismuth Dichalcogenides: Toward Earth-Abundant, Biocompatible Semiconductors. *J. Am. Chem. Soc.* **2018**, *140*, 3736−3742.
(38) Yang, C.; Wang, Z.; Wu, Y.; Lv, Y.; Zhou, B.; Zhang, W.-H. Synthesis, Characterization, and Photodetector Application of Alkali Metal Bismuth Chalcogenide Nanocrystals. *ACS Appl. Energy Mater.* **2019**, *2*, 182−186.
(39) Glemser, O.; Filcek, M. Über Alkalithiowismutate(III). *Z. Anorg. Allg. Chem.* **1955**, *279*, 321−323.
(40) McCarthy, T. J.; Tanzer, T. A.; Kanatzidis, M. G. A New Metastable Three-Dimensional Bismuth Sulfide with Large Tunnels: Synthesis, Structural Characterization, Ion-Exchange Properties, and Reactivity of KBi3S5. *J. Am. Chem. Soc.* **1995**, *117*, 1294.
(41) Kanatzidis, M. G.; McCarthy, T. J.; Tanzer, T. A.; Chen, L.-H.; Iordanidis, L.; Hogan, T.; Kannewurf, C. R.; Uher, C.; Chen, B. Synthesis and Thermoelectric Properties of the New Ternary Bismuth Sulfides KBi6.33S10 and K2Bi8S13. *Chem. Mater.* **1996**, *8*, 1465−1474.
(42) Davaasuren, B.; Alahmari, F.; Dashjav, E.; Khanderi, J.; Rothenberger, A. Synthesis and Characterization of the Ternary Thiobismuthates A9Bi13S24 (A = K, Rb). *Z. Anorg. Allg. Chem.* **2016**, *642*, 1480−1485.
(43) McClain, R.; Malliakas, C. D.; Shen, J.; He, J.; Wolverton, C.; González, G. B.; Kanatzidis, M. G. Mechanistic insight of $KBiQ_2$ (Q = S, Se) using panoramic synthesis towards synthesis-by-design. *Chem. Sci.* **2021**, *12*, 1378−1391.
(44) Hoang, K.; Mahanti, S. D. Atomic and electronic structures of I-V-VI2 ternary chalcogenides. *J. Sci. Adv. Mater. Dev.* **2016**, *1*, 51−56.
(45) Quarez, E.; Hsu, K.-F.; Pcionek, R.; Frangis, N.; Polychroniadis, E. K.; Kanatzidis, M. G. Nanostructuring, Compositional Fluctuations, and Atomic Ordering in the Thermoelectric Materials AgPbmSb-Te2+m. The Myth of Solid Solutions. *J. Am. Chem. Soc.* **2005**, *127*, 9177−9190.
(46) Morin, S. A.; Bierman, M. J.; Tong, J.; Jin, S. Mechanism and Kinetics of Spontaneous Nanotube Growth Driven by Screw Dislocations. *Science* **2010**, *328*, 476−480.
(47) Frank, F. C. Capillary equilibria of dislocated crystals. *Acta Crystallogr.* **1951**, *4*, 497−501.
(48) Eshelby, J. D. Screw Dislocations in Thin Rods. *J. Appl. Phys.* **1953**, *24*, 176−179.
(49) Burton, W. K.; Cabrera, N.; Frank, F. C.; Mott, N. F. The growth of crystals and the equilibrium structure of their surfaces. *Philos. Trans. R. Soc. Ser. A* **1951**, *243*, 299−358.
(50) Aramanda, S. K.; Chattopadhyay, K.; Choudhury, A. Exotic three-phase microstructures in the ternary Ag-Cu-Sb eutectic system. *Acta Mater.* **2021**, *221*, 117400.
(51) Singh, B.; Lin, H.; Prasad, R.; Bansil, A. Topological phase transition and quantum spin Hall state in TlBiS2. *J. Appl. Phys.* **2014**, *116*, 033704.
(52) Zhang, Q.; Cheng, Y.; Schwingenschlögl, U. Emergence of topological and topological crystalline phases in TlBiS2 and TlSbS2. *Sci. Rep.* **2015**, *5*, 8379.
(53) Antonius, G.; Louie, S. G. Temperature-Induced Topological Phase Transitions: Promoted versus Suppressed Nontrivial Topology. *Phys. Rev. Lett.* **2016**, *117*, 246401.
(54) Imai, T.; Chen, J.; Kato, K.; Kuroda, K.; Matsuda, T.; Kimura, A.; Miyamoto, K.; Eremeev, S. V.; Okuda, T. Experimental verification of a temperature-induced topological phase transition in $TlBiS_2$ and $TlBiSe_2$. *Phys. Rev. B* **2020**, *102*, 125151.
(55) Xu, S.-Y.; Xia, Y.; Wray, L. A.; Jia, S.; Meier, F.; Dil, J. H.; Osterwalder, J.; Slomski, B.; Bansil, A.; Lin, H.; Cava, R. J.; Hasan, M. Z. Topological Phase Transition and Texture Inversion in a Tunable Topological Insulator. *Science* **2011**, *332*, 560−564.

https://doi.org/10.1021/acs.cgd.2c00078
Cryst. Growth Des. 2022, 22, 3228−3234